Check for updates

Theoretical insight into hydroxyl production *via* H₂O₂ decomposition over the Fe₃O₄(311) surface†

Pin-Jun Lin, [a] Chen-Hao Yeh [ID] *[b] and Jyh-Chiang Jiang [ID] *[a]

Fenton's reagent provides a method to produce active hydroxyl radicals ($^{\bullet}OH$) for chemical oxidation by mixing iron oxide and hydrogen peroxide, which divides into homogeneous and heterogeneous Fenton's reagent. Heterogeneous Fenton's reagent is fabricated from H_2O_2 and various iron oxide solid materials, such as α-FeOOH, α-Fe$_2$O$_3$, and Fe$_3$O$_4$. Fe$_3$O$_4$ possesses the Fe^{2+}/Fe^{3+} mixed valence oxidational state and has been reported to have good catalytic activity. However, the reaction mechanism of H_2O_2 decomposition on Fe$_3$O$_4$ surfaces is still unclear. In this work, we performed DFT calculations to investigate the H_2O_2 decomposition mechanisms over the Fe$_3$O$_4$(311) surface. There are two iron environments for H_2O_2 adsorption and decomposition on the Fe$_3$O$_4$(311) surface, a Fe^{2+}/Fe^{3+} environment and a Fe^{3+}/Fe^{3+} environment. We found that the H_2O_2 can adsorb on the Fe^{2+}/Fe^{3+} environment by molecular adsorption but by dissociative adsorption on the Fe^{3+}/Fe^{3+} environment. Our results show that both adsorption structures can produce two OH groups on the Fe$_3$O$_4$(311) surface thermodynamically. In addition, based on the electronic property analysis, H_2O_2 on the Fe^{2+}/Fe^{3+} environment follows the Haber–Weiss mechanism to form one OH anion and one OH radical. On the other hand, H_2O_2 on the Fe^{3+}/Fe^{3+} environment follows the radical mechanism to form two OH radicals. In particular, the OH radical formed on Fe^{2+}/Fe^{3+} has energy levels on both sides of the Fermi energy level. It can be expected that this OH radical has good redox activity.

1. Introduction

Fenton's reagent is a well-known advanced oxidation process (AOP) that can produce reactive oxygen species (ROS), such as hydroxyl radicals ($^{\bullet}OH$), peroxyl radical ($^{\bullet}OOH$), and superoxide radical ($^{\bullet}O_2$).[1–4] Fenton's reagent is usually fabricated by mixing two solutions: a reducing transition metal and hydrogen peroxide. The Fenton-type reagent has been reported as an active catalyst for various reactions such as water treatment,[5,6] methane partial oxidation, and mercury removal. Most AOPs can damage the organic compounds into H_2O, CO_2, and other small molecules by means of hydroxyl radicals ($^{\bullet}OH$) because of their strong oxidative ability.[7] As one of the well-known AOPs, the Fenton reagent shows extraordinary ability for organic decomposition and the least expensive. Moreover, the development of a Fenton reaction can accelerate the application of AOPs for water treatment and purification on an industrial scale.

Conventional homogeneous Fenton reagent composed of hydrogen peroxide (H_2O_2) and ferrous ion (Fe^{2+}) for the purpose of producing hydroxyl radicals.[8] However, there are several drawbacks to the homogeneous Fenton reagent.[9] For example, homogeneous Fenton reagent needs to react in the narrow pH range, and the aggregation of iron-containing sludge in the reaction can also limit the recycling of catalysts, which can be considered as secondary pollution in the environment.[10,11] Compared to the homogeneous Fenton systems, the heterogeneous iron-based solid catalysts can serve as the other choices for the Fenton reagents, which have been reported in various previous studies.[12] Iron oxides-based catalysts, such as α-FeOOH, α-Fe$_2$O$_3$, Fe$_3$O$_4$, and FeO,[13–17] possess good catalytic properties in many heterogeneous catalysis reactions, including Fenton reaction[18] and Fischer–Tropsch synthesis.[19] Theoretically, Song *et al.* has reported the NO oxidation mechanism over α-Fe$_2$O$_3$ catalyst by H_2O_2.[20] Experimentally, Li *et al.* have studied the α-FeOOH material as the pCNB degradation catalyst by Fenton-like process.[21] Furthermore, several investigations have found that the mixed valence oxidational state of iron atoms possess unique catalytic activity towards many heterogeneous catalysis reactions, including Fenton reaction, methane partial oxidation, and mercury oxidation.[10,22–27] Among, magnetite (Fe$_3$O$_4$) is one of the iron oxide material that has a Fe^{2+}/Fe^{3+} mix valence oxidational state. The bulk magnetite crystal structure was a member of the inverse cubic spinel group with the ferrimagnetic property.[28,29]

[a] Department of Chemical Engineering, National Taiwan University of Science and Technology, No. 43, Keelung Rd., Sec. 4, Da'an Dist., Taipei 10607, Taiwan. E-mail: jcjiang@mail.ntust.edu.tw

[b] Department of Materials Science and Engineering, Feng Chia University, No. 100, Wenhwa Rd., Seatwen, Taichung, 40724, Taiwan. E-mail: chenhyeh@fcu.edu.tw

There are many applications of using magnetite as pigment due to its magnetic properties, such as polishing compounds, cosmetics, medicines, polymer, and rubber filler.[30–32]

There are still some challenges for heterogeneous Fenton reagents, such as that the yield to produce the OH radical is low. In addition, the mechanism to produce the OH radical *via* heterogeneously mixed valence iron oxide catalysts such as Fe_3O_4 of the Fenton reaction is unclear. In literature, there have been proposed two possible mechanisms for the traditional Fenton reaction. The first mechanism had been proposed by Haber and Weiss in the 1930s, named hydroxyl free radical mechanism (Haber–Weiss mechanism),[8] which involves the formation of hydroxyl radicals (˙OH) in the system with the ferry (Fe^{2+}) oxidation. This radical mechanism for the Fenton reaction with the following elementary reactions.

$$Fe^{2+} + H_2O_2 \rightarrow Fe^{3+} + \cdot OH + OH^-$$

$$Fe^{3+} + H_2O_2 \rightarrow Fe^{2+} + \cdot OOH + H^+$$

Thereafter, another mechanism was proposed by Bray and Gorin in 1932,[33] which generate higher valence Fe complexes such as ferryl (Fe^{IV}) ion in the Fenton system, as follows:

$$Fe^{2+} + H_2O_2 \rightarrow Fe^{IV}O + H_2O$$

$$Fe^{IV}O + H_2O_2 \rightarrow Fe^{2+} + H_2O + O_2$$
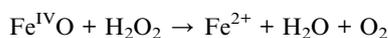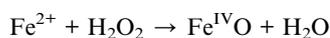
As a structure in the spinel family, Fe_3O_4 also possesses stable low-index surfaces, (100), (110), (111) facets,[34–37] and a high-index surface of (311). Some studies have been reported the mercury oxidation mechanism by H_2O_2 over Fe_3O_4(001) and Fe_3O_4(111) surfaces.[27,38] However, even though the low-index facets have relatively low surface energies, Xu *et al.* have successfully synthesized a polyhedral 50-facet Fe_3O_4 nanocrystal where only one high-index Fe_3O_4(311) facet can stably exist with other low-index facets jointly.[39] In their results, there were even 24 high-index (311) facets in that nanocrystal, which is stable and abundant. Thus, Fe_3O_4(311) facet is a stable high-index surface experimentally. Because there was no investigation on the mechanism of the Fenton reaction over the Fe_3O_4(311) surface, in this work, we studied the adsorption and decomposition of H_2O_2 (Fenton reaction) over Fe_3O_4(311) surface using DFT calculations. We also investigated the possible reaction mechanisms of the Fenton reaction on the Fe_3O_4(311) surface. Moreover, we analyzed the electron density difference (EDD) and density of states (DOS) to explore the electronic interaction between H_2O_2/OH and Fe_3O_4(311) surface. To clarify the oxidational states of iron atoms between H_2O_2/OH and Fe_3O_4(311) surface, we also calculated the Bader charge and magnetic moments for the iron atoms on the Fe_3O_4(311) surface.

2. Computational details

The spin-polarized periodic DFT calculations were carried out with the Vienna *ab initio* simulation package (VASP 5.4.1).[40–43]

The generalized gradient approximation (GGA) with the functional proposed by Perdew, Burke and Enzerhof (PBE) exchange-correlation functional[44] was used together with a plane-wave basis set with a kinetic cutoff energy of 500 eV. The electron ion–core interactions were described by the projector augmented wave (PAW) method.[45,46] In order to correctly describe the itinerant or localized behavior of the Fe 3d-orbital, it is important to account for the strong on-site Coulomb correlations.[47,48] Therefore, in this work, all systems were calculated by using the Hubbard correction term U (GGA + U). We applied the rotationally invariant approach proposed by Dudarev *et al.* with an effective Hubbard parameter of 4.0 eV for iron, which is the difference between the Coulomb (U) and exchange (J) parameters ($U_{eff} = U - J$). The optimized exchange-correlation functional (optB86b-vdW) was considered to determine the effect of van der Waals interactions.[49]

For the total energy calculations, the Brillouin zone integrations for the pristine and defect system were performed using the $2 \times 2 \times 1$ based on the Monkhorst–Pack k-points scheme[50] for all structural configuration relaxations. The convergence threshold was set to be 10^{-5} eV for electronic optimization and the force convergence was set to be 0.02 eV $Å^{-1}$ for structural optimization. The adsorption energy (E_{ads}) of adsorbate was defined as following equation:

$$E_{ads} = E_{Total} - E_{surf.} - E_{Molecule}$$

where E_{Total} is the total energy of the surface together with the adsorbate, $E_{surf.}$ is the total energy of the surface, and $E_{molecule}$ is the total energy of the free molecule in gas-phase. Therefore, a negative adsorption energy illustrated a thermodynamically-favored exothermic adsorption process. An $8 \times 8 \times 1$ k-point grid was used to calculate electronic density difference (EDD), Bader charge analysis, and density of state (DOS) with the same cutoff energy. The climbing image nudged elastic band (CI-NEB) method[51] and dimer method was applied to find transition states and minimum energy path of all reactions. The vibrational frequencies analysis was performed for validating the optimized and transition state structures.

The bulk Fe_3O_4 was adopted the conventional Fe_3O_4 unit cell comprising 56 atoms ($Fe_{24}O_{32}$). For the Fe_3O_4 bulk calculations, $8 \times 8 \times 8$ k-mesh of a grid density was employed. The optimized lattice parameters of bulk Fe_3O_4 were $a = b = c = 8.396$ Å and $\alpha = \beta = \gamma = 90°$. The result of the calculation is in good agreement well with the experimental data ($a = b = c = 8.394$ Å and $\alpha = \beta = \gamma = 90°$).[52] The bulk magnetite crystal structure was inverse cubic spinel with ferrimagnet property, the structure comprises the tetrahedral iron site and octahedral iron site with different oxidation number, and the O anions form a close-packed face-centered cubic (fcc) sublattice, as shown in Fig. S1(a).† Moreover, the tetrahedral and octahedral iron sites were performed by two magnetic sub-lattices in the opposite direction to form a typical inverse spinel structure as $[Fe^{3+}]_{tet}[Fe^{3+}, Fe^{2+}]_{oct}O_4$. During the calculation, the initial atomic spin magnetic moments were $m_s = -5$ μ_B and 4 μ_B for the tetrahedral iron and the octahedral iron sites, respectively. After structure optimization, the magnetic moment per formula unit was

calculated to be 4.0 μ_B, which lies close to experiment data (4.05 μ_B).[32] The magnetic moments of Fe^{3+} and Fe^{2+} in the tetrahedral iron and the octahedral iron atoms were with the antiparallel alignment, creating the ferrimagnetic character. Fig. S1(b)† shows the structure of the Fe_3O_4(311) surface by constructing four molecular layer models with the bottom two layers being fully fixed. The simulated XRD pattern of Fe_3O_4 bulk structure is drawn in Fig. S1(c),† which is in a good agreement with the experimental observation.[53]

3. Results and discussion

3.1 Adsorption of H_2O_2 molecule

Fig. 1 shows the adsorption configuration of H_2O_2 on the Fe_3O_4(311) surface. There are two possible adsorption structures of H_2O_2 on the Fe_3O_4(311) surface: (1) molecular adsorption (Fig. 1(a)) and (2) dissociative adsorption (Fig. 1(b)). In the H_2O_2 molecular adsorption structure, the H_2O_2 adsorbs on the Fe_{tet} site *via* one OH to form the Fe–O bond, while the other OH end of H_2O_2 points to the lattice oxygen to form the hydrogen bond instead of forming the Fe–O bond between the adjacent Fe_{oct} site, as can be seen in Fig. 1(a). The adsorption energy of the H_2O_2 molecular adsorption is −1.17 eV. Moreover, the molecule geometry of H_2O_2 distorts seriously after adsorption that the two OH bonds within the molecule point to the different lattice oxygen atoms and form the hydrogen bonding with the distances of 1.66 Å and 1.47 Å, respectively. It results in the O–H bonds within the molecule elongated from 0.98 Å (free H_2O_2) to 1.016 and 1.061 Å, respectively. In the dissociative adsorption of H_2O_2, the H_2O_2 adsorbs on the two adjacent Fe_{oct} sites to form two Fe–O bonds, with the whole O–O bond being paralleled to the bridge of two octahedral iron sites, and one O–H bond directly dissociates to form OOH group, as can be

seen in Fig. 1(b). The adsorption energy of H_2O_2 dissociative adsorption is −1.56 eV. The O–O bond of the OOH is elongated from 1.472 Å (in free H_2O_2) to 1.483 Å, as listed in Table 1.

3.2 The activation of H_2O_2 on Fe_3O_4

To understand the reaction mechanism of H_2O_2 decomposition, we calculated the energy barrier and reaction energy of each reaction step from both adsorption structures of H_2O_2 on the Fe_3O_4(311) surface. Two cleave aspects are considered in either molecular adsorption of H_2O_2 or dissociative adsorption of H_2O_2: (1) O–O bond-breaking into the OH group; (2) O–H bond-breaking into the OOH group. The following steps show the possible mechanisms for the molecular adsorption of H_2O_2 on the Fe_3O_4(311) surface:

$$H_2O_2 \rightarrow 2OH \tag{1}$$

$$H_2O_2 \rightarrow OOH + H \tag{2}$$

$$OOH \rightarrow OH + O \tag{3}$$

In eqn (1), the reaction barrier is 0.76 eV of that the H_2O_2 molecule cleaves the O–O bond to form two OH groups on one Fe_{tet} site and one Fe_{oct} site, and the reaction energy of this reaction is significant exothermic by 1.44 eV. Fig. S2(a)† depicts the structures of the initial state, transition state, and final state of this reaction. In eqn (2), the pathway starts from the deprotonation of H_2O_2 to deliver one hydrogen atom to the lattice oxygen, then forming an OOH group and the surface hydroxyl group. The oxygen atoms of the OOH group are separately adsorbed on both Fe_{tet} and Fe_{oct}, as shown in Fig. S2(b).† The calculated energy barrier of this reaction is 0.52 eV by a slight endothermicity of 0.22 eV. Comparing the pathways *via* O–O bond breaking and deprotonation, the reaction in the former is more thermodynamically favorable to produce the two OH groups, but it has larger activation energy for O–O bond scission, whereas the reaction in the latter possesses a smaller energy barrier to form the OOH group.

When the decomposition reaction starts from the dissociative adsorption of H_2O_2 (H + OOH), the reaction can also divide into O–O bond breaking and OH deprotonation reactions. The first pathway is the O–O bond decomposition of OOH to form O atom and OH group on two Fe_{oct} sites of the surface. The calculated energy barrier and reaction energy of this elementary step (OOH → O + OH) is 0.24 eV and 0.20 eV, respectively. The activated O–O bond length in the transition state structure is 1.70 Å, and the intermediate state will form a hydrogen bonding interaction between the O atom and OH group with a distance of 1.86 Å after dissociation, as shown in Fig. S3(a).† However, the dissociated O atom is unstable so that this O atom can attract the atomic H of the surface hydroxyl group to form another OH group on the Fe_{oct2} site *via* the hydrogen bonding networks, which results in a large exothermic reaction by 1.44 eV due to the stability of forming two OH groups. The second pathway is that deprotonation from OOH to transfer one H atom to the lattice oxygen to form dioxygen on the two octahedral iron sites, as shown in Fig. S3(b).† This process is
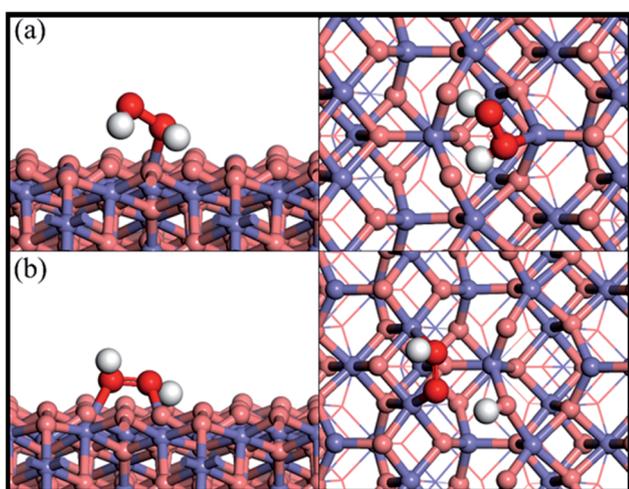

Fig. 1 Side and top views of optimized adsorption structures of H_2O_2 on the Fe_3O_4(311) surface by different adsorption configurations of (a) molecular adsorption and (b) dissociative adsorption. Purple, red, and white spheres represent Fe, O, and H atoms, respectively. The deep red color represents the oxygen of H_2O_2 while the light red color is the oxygen of Fe_3O_4(311) surface.

Table 1 The adsorption energy and geometrical parameters of H_2O_2 via different adsorption configurations on the Fe_3O_4(311) surface

Adsorption type	E_{ads} (eV)	O–O bond length (Å)	O–H_1 bond length (Å)	O–H_2 bond length (Å)
Gas phase	—	1.472	0.98	0.98
Molecular adsorption	−1.17	1.475	1.016	1.061
Dissociate adsorption	−1.57	1.483	2.135	0.983

Table 2 Calculated reaction barriers (E_a in eV), reaction energies (ΔE in eV), and imaginary frequencies (IMF, cm^{-1}) for elementary reactions of H_2O_2 decomposition on the Fe_3O_4(311) surface

Elementary steps	E_a	ΔE	IMF (cm^{-1})
Molecular adsorption			
$H_2O_{2(gas)} \rightarrow H_2O_2^*$	—	−1.17	
$H_2O_2^* \rightarrow 2OH^*$	0.76	−1.44	i424
$H_2O_2^* \rightarrow H^* + OOH^*$	0.52	0.22	i493
Dissociate adsorption			
$H_2O_2^*_{(gas)} \rightarrow H^* + OOH^*$	—	−1.57	
$H^* + OOH^* \rightarrow H^* + O^* + OH^*$	0.24	0.20	i641
$H^* + O^* + OH^* \rightarrow 2OH^*$	—	−1.44	
$H^* + OOH^* \rightarrow OO^* + 2H^*$	0.79	0.002	i943

a thermal neutral process with an activation energy of 0.79 eV. This result demonstrates that the most favorable pathway from the decomposition reaction of the dissociative adsorption of H_2O_2 is to produce two OH groups on the Fe_3O_4(311) surface. Table 2 summarizes the calculated reaction energy and activated barriers of the elementary steps of the O–O bond and O–H bond dissociation of H_2O_2 on Fe_3O_4(311) surface. Fig. 2 depicts the potential energy profiles for H_2O_2 decomposition on

different sites over Fe_3O_4(311) surface. Our results show that it is thermodynamically favorable to produce the two hydroxyl groups on the Fe_3O_4(311) surface from both molecular adsorption and dissociative adsorption.

3.3 Solvent effect

To realistically simulate the effect of the catalytic environment on Fenton's reaction, we carried out the implicit solvent model by using VASPsol.[54,55] The implicit solvent effect of water was adopted in this work, where the corresponding dielectric constant of water was 78.3553. As listed in Table S1,† the reaction barriers of either O–O bond breaking or O–H bond breaking of the H_2O_2 molecule in an aqueous solution become smaller than that of the H_2O_2 molecule in the vacuum, which is contributed by the solvent effects. Besides, the OH groups production is still the most thermodynamically favorable pathway via O–O bond breaking of the H_2O_2 on the Fe_3O_4(311) surface, as shown in Fig. S4.† Thus, with/without the solvent effect, the reaction trend of H_2O_2 decomposition on the Fe_3O_4(311) surface is similar.

3.4 Electronic property analysis

3.4.1 H_2O_2 molecular adsorption. To analyze the interactions between H_2O_2 and Fe atoms upon adsorption on
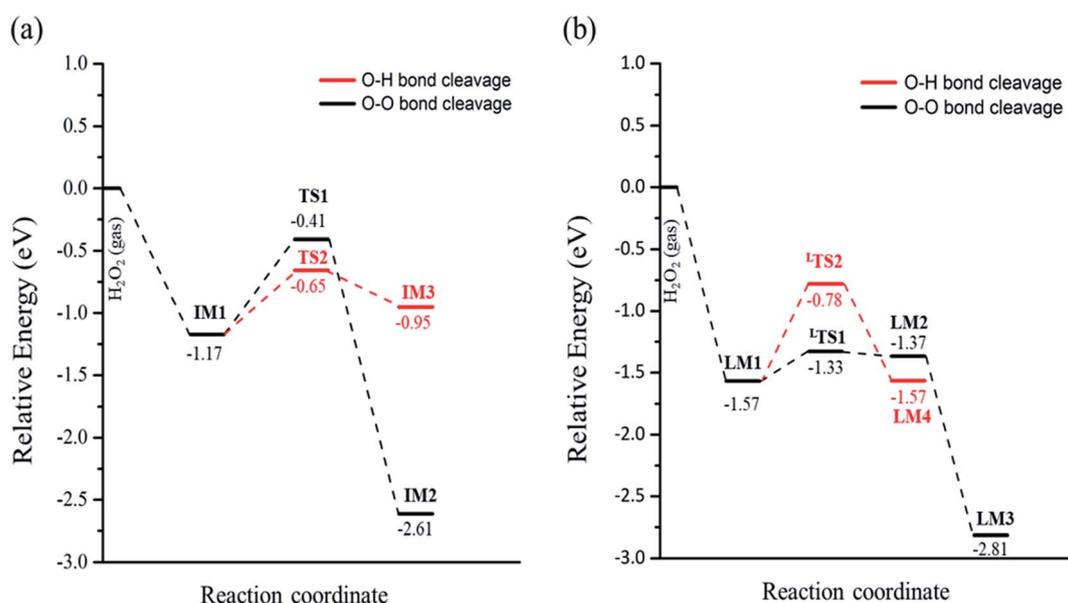

Fig. 2 The potential energy profiles of the decomposition of H_2O_2 on the Fe_3O_4(311) surface via (a) H_2O_2 molecular adsorption and (b) H_2O_2 dissociative adsorption.
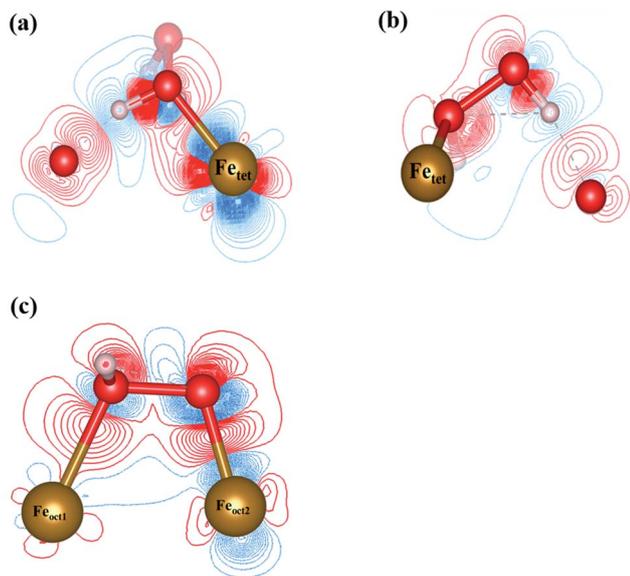
Fig. 3 The 2D electron density difference diagrams of (a) Fe_{tet}−OH−O plane, and (b) Fe_{tet}−O−O plane of H_2O_2 molecular adsorption, and (c) H_2O_2 dissociative adsorption. The isosurface level is $0.002|e|/bohr^3$. Brown, red, and white spheres represent Fe, O, and H atoms, respectively.

$Fe_3O_4(311)$ surface, we calculate the electron density difference (EDD) and density of states (DOS). Fig. 3(a) and (b)† show the different views of 2D EDD contour plots of H_2O_2 molecular

adsorption. Fig. 3(a) illustrates the accumulation of electron region between the OH group and Fe_{tet} site, representing that the oxygen donates electrons to the iron atom to form a dative bond between oxygen and iron atom. On the other hand, Fig. 3(b) shows the cutting plane along with the other H atom and the O–O bond (H_t–O–O), which displays the electron density accumulation (red contour) between the OH group and the lattice O. This EDD plot in Fig. 3(b) indicates that the H_2O_2 donates the electron transfer from the lattice O to the OH group *via* the hydrogen bonding interaction. In addition, Fig. 4(a) shows the PDOS diagram of the H_2O_2 molecule before and after its adsorption. One can observe that the spin up and spin down of the peaks of H_2O_2 is getting splitting after adsorption. Moreover, as can be seen in Fig. S5(a) and (b),† the projected d orbitals of Fe_{tet} and Fe_{oct} atoms show that the d orbitals of Fe_{tet} have obviously changed, and the peak is getting broad. In comparison, the peaks of the Fe_{oct} changed slightly after H_2O_2 adsorption. Additionally, the d orbitals of the Fe_{tet} atom have an overlap with the p orbitals of H_2O_2 around −0.50 eV, reflecting the dative bond between H_2O_2 and Fe_{tet} atom.

3.4.2 H_2O_2 dissociative adsorption. Fig. 3(c) shows the 2D EDD plot of the OOH group of the H_2O_2 dissociative adsorption configuration, and the cutting plane is along the bridge between two Fe_{oct} atoms and the O–O bond (Fe_{oct}–O–O–Fe_{oct}). The blue contour around the OOH group reveals that the OOH group loses electrons electron. There is also a broad electron density accumulation (red contour) around the bound OOH and two
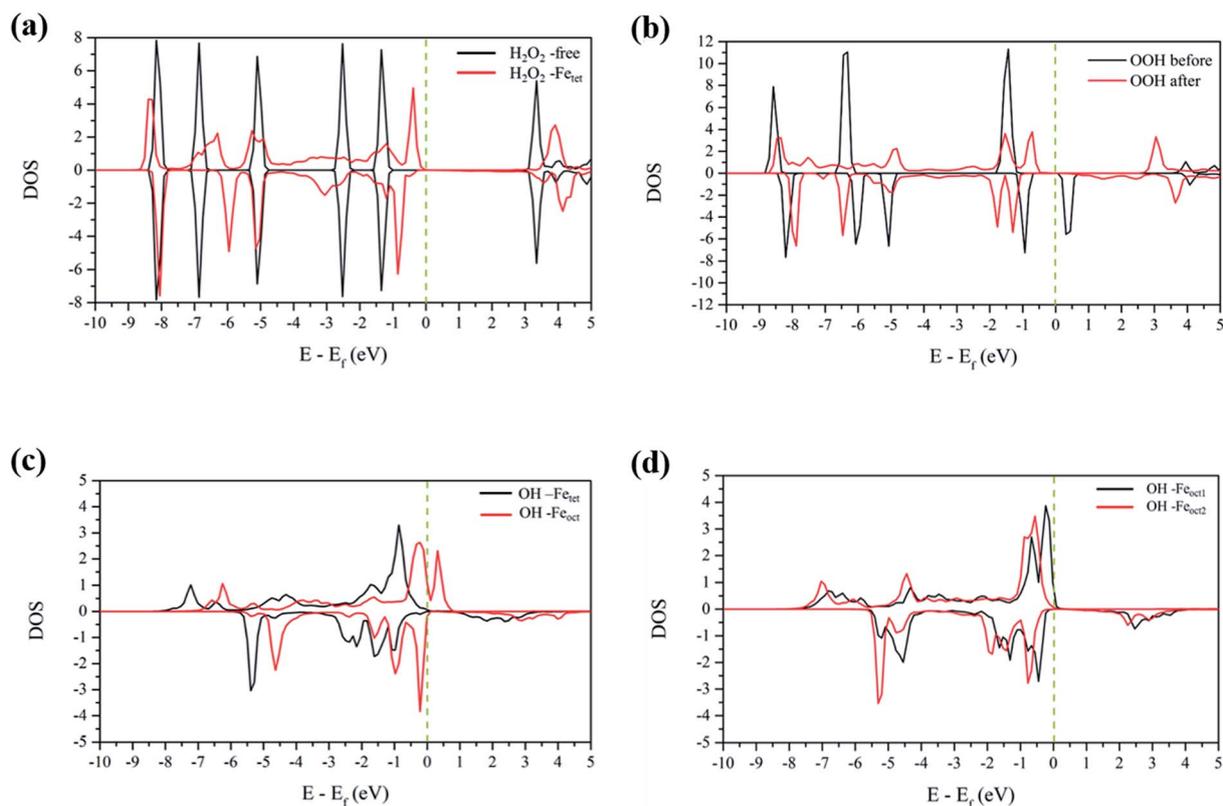

Fig. 4 The PDOS plots of (a) H_2O_2 before and after molecular adsorption, (b) H_2O_2 before and after dissociative adsorption, (c) OH groups from the decomposition of H_2O_2 molecular adsorption, and (d) OH groups from the decomposition of H_2O_2 dissociative adsorption. The dotted line is the Fermi level.

Fe$_{oct}$ atoms, and the region around the OOH group, which indicates the strong electron interactions between Fe atoms and the OOH group. The strong electronic interactions mean that the OOH can form a dative chemical bond with the Fe atoms.

Further, the PDOS plots, as shown in Fig. 4(b), demonstrated that the peaks of the OOH (from the dissociative adsorption of H$_2$O$_2$) has a significant splitting on both spin up and spin down, reflecting the strong radical property of the OOH group. The peaks around −1.50 eV and −1.00 eV belong to α-HOMO and β-HOMO, respectively, as well as the peak around 0.50 eV represents the LUMO of the OOH group before adsorption (black line in Fig. 4(b)). For the dissociative adsorption configuration of H$_2$O$_2$, the peaks of the OOH group (red line in Fig. 4(a)) display a broad region above Fermi level energy to 3.00 eV, but the peaks around 0.50 eV disappear. It reflects that the OOH group can gain electrons from the Fe atoms. After dissociative adsorption configuration of H$_2$O$_2$, the peaks still show a notable splitting on both spin up and spin down, representing the strong radical property of the OOH group. Besides, as can be seen in Fig. S5(c) and (d),† the d orbital of the Fe$_{oct2}$ atom shows a more remarkable change than that of the Fe$_{oct1}$ atom before and after OOH group formation, indicating the strong interaction between the Fe$_{oct2}$ atom and the OOH group.

3.4.3 OH on the Fe$_{tet}$/Fe$_{oct}$ of the Fe$_3$O$_4$(311) surface. According to the calculated results, both molecular adsorption of H$_2$O$_2$ and dissociative adsorption of H$_2$O$_2$ can produce two OH groups on either Fe$_{oct}$ or Fe$_{tet}$ atoms of the Fe$_3$O$_4$(311) surface. Because Fenton's reaction involves the redox reaction, we did the electronic property analysis to understand the electronic and magnetic properties after H$_2$O$_2$ decomposition. Fig. S6(a) and (b)† show the EDD plots of the adsorption of the OH group on the Fe$_{oct}$ and Fe$_{tet}$ sites after H$_2$O$_2$ decomposition, respectively. It shows wide regions of electron density accumulation (red lines) between the OH group and either Fe$_{tet}$ or Fe$_{oct}$ atoms, which shows the electron transferred from the OH group to the Fe atoms. Fig. 4(c) represents the PDOS of the OH groups on the Fe$_{tet}$ and Fe$_{oct}$ sites after H$_2$O$_2$ decomposition. For the OH on the Fe$_{oct}$ atom, there are peaks with similar intensity on both sides of the Fermi level, indicating that the oxygen atom on OH has unpaired electrons after H$_2$O$_2$

decomposition. Since the peaks are close to the Fermi level, we can expect that the OH group on the Fe$_{oct}$ atom should be very active. Besides, it can be observed from Fig. S7(a)† that the DOS distribution of Fe$_{tet}$ changes significantly before and after adsorption, whereas from Fig. S7(b)† that the DOS distribution of Fe$_{oct}$ is very similar after H$_2$O$_2$ decomposition. The changes of the DOS distribution of Fe$_{tet}$ implies that Fe$_{tet}^{2+}$ might have been oxidized to Fe$_{tet}^{3+}$.

To further understand the redox reaction before and after H$_2$O$_2$ decomposition on the Fe$_3$O$_4$(311) surface, we calculated the Bader charge and magnetic moments of iron ions and the fragments of H$_2$O$_2$ during the reaction. The calculated Bader charge values and magnetic moment values of iron ions are similar before and after the adsorption of H$_2$O$_2$. After the adsorption of H$_2$O$_2$, the calculated Bader charge values of Fe$_{tet}$ and Fe$_{oct}$ are around 1.36 and 1.67|e|, respectively, and the calculated magnetic moment values of both Fe$_{tet}$ and Fe$_{oct}$ atoms are around 3.804 and 4.243 μ_B, respectively. The results indicate that the oxidational state of Fe$_{tet}$ and Fe$_{oct}$ atoms upon H$_2$O$_2$ adsorption is Fe^{2+} and Fe^{3+}, respectively. Furthermore, after the H$_2$O$_2$ decomposition to OH groups, the calculated Bader charge value of both Fe$_{tet}$ and Fe$_{oct}$ atoms become 1.69 and 1.71|e|, respectively, and the calculated magnetic moment of both Fe$_{tet}$ and Fe$_{oct}$ atoms become 4.249 and 4.234 μ_B, respectively, as listed in Table 3. The changes in Bader charge and the magnetic moment suggest that the Fe$_{tet}$ is oxidized from Fe^{2+} to Fe^{3+}, while the Fe$_{oct}$ is maintained at Fe^{3+}. The calculated results indicate that the OH group on the Fe$_{tet}$ will be reduced to the OH$^-$ anion, while the one on the Fe$_{oct}$ will be an OH radical, which is consistent with the prediction of DOS analysis. Therefore, we predict that the Fe$_{tet}$ and Fe$_{oct}$ atoms may be the ferrous ion (Fe^{2+}) and ferric ion (Fe^{3+}) initially and then the Fe$_{tet}$ can be oxidized to Fe^{3+} after H$_2$O$_2$ decomposition, in agreement with the prediction from PDOS analysis. As a result, we predict that this redox mechanism follows the Haber–Weiss mechanism of the Fenton's reaction as the following equations:

$$H_2O_2 \rightarrow {}^\cdot OH + {}^\cdot OH$$

$$Fe_{tet}^{2+} + {}^\cdot OH \rightarrow Fe_{tet}^{3+} + OH^-$$
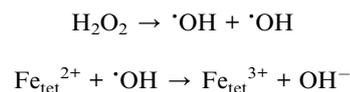
Table 3 Calculated Bader charge and magnetization for Fe atoms, H$_2$O$_2$, and OH groups before and after H$_2$O$_2$ decomposition. The positive and negative values of the Bader charge represent the loss and gain electrons, respectively

Species	Bader charge	Magnetization	Species	Bader charge	magnetization
Free surface			Free surface		
Fe$_{tet}$	1.32	3.782	Fe$_{oct1}$	1.68	4.248
Fe$_{oct}$	1.67	4.240	Fe$_{oct2}$	1.69	4.262
Molecular adsorption			Dissociative adsorption		
Fe$_{tet}$	1.36	3.804	Fe$_{oct1}$	1.73	4.258
Fe$_{oct}$	1.67	4.243	Fe$_{oct2}$	1.71	4.276
H$_2$O$_2$	−0.012	—	H–OOH	−0.09	—
OH on the Fe$_{tet}$/Fe$_{oct}$			OH on the Fe$_{oct1}$/Fe$_{oct2}$		
Fe$_{tet}$	1.69	4.249	Fe$_{oct1}$	1.69	4.258
Fe$_{oct}$	1.71	4.234	Fe$_{oct2}$	1.70	4.278
OH–Fe$_{tet}$	−0.47	—	OH–Fe$_{oct1}$	−0.50	—
OH–Fe$_{oct}$	−0.51	—	OH–Fe$_{oct2}$	−0.45	—

$$Fe_{oct}^{3+} + {}^{\cdot}OH \rightarrow Fe_{oct}^{3+} + {}^{\cdot}OH$$
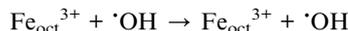
3.4.4   OH on the Fe$_{oct1}$/Fe$_{oct2}$ of the Fe$_3$O$_4$(311) surface.
After the decomposition of the H$_2$O$_2$ to two OH groups on the Fe$_{oct1}$ and Fe$_{oct2}$ atoms, we also investigated the electronic interaction between these OH groups and the Fe$_{oct}$ atoms *via* EDD, PDOS, Bader charge and magnetization analyses. Fig. S6(c) and (d)† show the EDD contour plots from the different perspective cutting planes of these two OH groups. These EDD plots display a wide region with electron density accumulation (red color) between the OH group and either Fe$_{oct1}$ or Fe$_{oct2}$ atoms, demonstrating the OH group has a strong interaction with either Fe$_{oct1}$ or Fe$_{oct2}$ atoms. In Fig. 4(d), the peaks of OH groups show a little split, which also denotes the radical character for these OH groups. Besides, the PDOS of the d orbital of either Fe$_{oct1}$ atom or Fe$_{oct2}$ atom display only slightly changes before and after H$_2$O$_2$ decomposition, as shown in Fig. S7(c) and (d).† This result implies that the redox reactivity between OH groups and Fe$_{oct1}$/Fe$_{oct2}$ atoms is weak.

The calculated Bader charge values have slight changes on both Fe$_{oct1}$ and Fe$_{oct2}$ atoms before and after O–O decomposition, where the value of Fe$_{oct1}$ atom changes from 1.68$|e|$ to 1.73$|e|$, and the value of Fe$_{oct2}$ atom from 1.69$|e|$ becomes 1.71$|e|$. The calculated magnetic moment values of both Fe$_{oct1}$ and Fe$_{oct2}$ atoms remain around 4.25 μ_B before and after O–O decomposition. These results indicate that both Fe$_{oct1}$ and Fe$_{oct2}$ atoms are the ferric ions (Fe^{3+}) initially and the Fe atoms will get hardly further oxidized after forming the OH group on these Fe atoms. Thus, the OH groups on these ferric ions (Fe^{3+}) also possess a radical character after H$_2$O$_2$ decomposition. The calculated Bader charge and magnetic moment values are listed in Table 3.

Finally, in a comparison of two mechanisms of H$_2$O$_2$ decomposition on the Fe$_3$O$_4$(311) surface, we found that it can occur a redox reaction between H$_2$O$_2$ and Fe$_3$O$_4$(311) surface when H$_2$O$_2$ adsorbed on both Fe$_{tet}$ and Fe$_{oct}$ sites. The mechanism obeys the Haber–Weiss mechanism to produce one OH anion and one OH radical, which has a strong redox activity. On the other hand, while H$_2$O$_2$ adsorbed on two Fe$_{oct}$ sites, H$_2$O$_2$ can dissociate into two OH radicals without oxidizing the Fe$_{oct}$ atoms, which is the radical mechanism of H$_2$O$_2$ decomposition. Based on these results, we could predict that the active OH radicals would be the surface abundant species on the Fe$_3$O$_4$(311) surface. Moreover, the calculated desorption energies of OH radicals are 2.84 eV and 2.94 eV at Fe$_{tet}^{2+}$/Fe$_{oct}^{3+}$ and Fe$_{oct}^{3+}$/Fe$_{oct}^{3+}$ sites, respectively. The desorption energy indicated that the hydroxyl radicals might be challenging to desorb from the Fe$_3$O$_4$(311) surface. Therefore, in our study, we predict that the surface OH groups might go through surface heterogeneous oxidation reactions.

4.   Conclusions

In this work, we have employed DFT calculations to study the H$_2$O$_2$ adsorption and the decomposition mechanism on the Fe$_3$O$_4$(311) surface. Fe$_3$O$_4$(311) surface possesses a mixed

valence (Fe^{2+}/Fe^{3+}) state so that there are two possible adsorption sites for H$_2$O$_2$ adsorption. When H$_2$O$_2$ adsorbs on the Fe$_{tet}^{2+}$/Fe$_{oct}^{3+}$ sites, the adsorption structure is molecular adsorption, whereas the adsorption structure of H$_2$O$_2$ on Fe$_{oct}^{3+}$/Fe$_{oct}^{3+}$ sites becomes dissociative adsorption (OOH + H). We found that the molecular adsorption of H$_2$O$_2$ can proceed O–H or O–O bond scission to form OOH or 2OH on the Fe$_3$O$_4$(311) surface, respectively. The O–H and O–O bond dissociation is kinetic control and thermodynamic control of the decomposition reaction for the molecular adsorption of H$_2$O$_2$, respectively. On the contrary, the dissociative adsorption of H$_2$O$_2$ only prefers to go through the O–O bond scission to produce 2OH on the Fe$_3$O$_4$(311) surface with a small energy barrier of 0.24 eV. In addition, according to various electronic property calculations, DOS, EDD, Bader charge, and magnetic moments, we observed that the reaction from H$_2$O$_2$ to 2OH on the Fe$_{tet}^{2+}$/Fe$_{oct}^{3+}$ sites obeys the Haber–Weiss mechanism of the Fenton reaction. The Fe$_{tet}^{2+}$ site can be oxidized to Fe$_{tet}^{3+}$ while the other Fe$_{oct}^{3+}$ site maintains its original oxidation state. Thus, the 2OH formed from the molecular adsorption of H$_2$O$_2$ is a composition of OH anion and OH radical. On the contrary, the 2OH produced from the dissociative adsorption of H$_2$O$_2$ is two radicals because the Fe$_{oct}^{3+}$/Fe$_{oct}^{3+}$ sites did not change their oxidation states, which belongs to the radical mechanism. Compared to two mechanisms, it can produce an active OH radical on the surface *via* either the Haber–Weiss mechanism or radical mechanism, where the oxidation state of Fe on the Fe$_3$O$_4$(311) surface can stay at Fe^{3+} instead of further oxidation. As a result, our results predict that these OH radicals from the Fenton-like reaction of H$_2$O$_2$ on the Fe$_3$O$_4$(311) surface might be a candidate of oxidant for other heterogeneous catalysis reactions.

Conflicts of interest

There are no conflicts to declare.

Acknowledgements

References

1 R.-S. Juang, S.-H. Lin and T.-Y. Wang, *Chemosphere*, 2003, **53**, 1221–1228.

2 B. Durham, M. M. Bourbigot and T. Pankratz, *Desalination*, 2001, **138**, 83–90.

3 F. Fu and Q. Wang, *J. Environ. Manage.*, 2011, **92**, 407–418.

4 I. Zinicovscaia, in *Cyanobacteria for Bioremediation of Wastewaters*, ed. I. Zinicovscaia and L. Cepoi, Springer

International Publishing, Cham, 2016, pp. 17–25, DOI: 10.1007/978-3-319-26751-7_3.

5 W. H. Glaze, *Environ. Sci. Technol.*, 1987, **21**, 224–230.

6 C. P. Huang, C. Dong and Z. Tang, *J. Waste Manage.*, 1993, **13**, 361–377.

7 K. Keyer, A. S. Gort and J. A. Imlay, *J. Bacteriol.*, 1995, **177**, 6782.

8 F. Haber and J. Weiss, *Naturwissenschaften*, 1932, **20**, 948–950.

9 Y. F. Huang and Y. H. Huang, *J. Hazard. Mater.*, 2009, **162**, 1211–1216.

10 Y. Yao, L. Wang, L. Sun, S. Zhu, Z. Huang, Y. Mao, W. Lu and W. Chen, *Chem. Eng. Sci.*, 2013, **101**, 424–431.

11 M. Zhou, Q. Yu, L. Lei and G. Barton, *Sep. Purif. Technol.*, 2007, **57**, 380–387.

12 S. Rahim Pouran, A. A. Abdul Raman and W. M. A. Wan Daud, *J. Cleaner Prod.*, 2014, **64**, 24–35.

13 Z. Ai, Y. Cheng, L. Zhang and J. Qiu, *Environ. Sci. Technol.*, 2008, **42**, 6955–6960.

14 R. Huang, Z. Fang, X. Yan and W. Cheng, *Chem. Eng. J.*, 2012, **197**, 242–249.

15 K. Rajeshwar, M. E. Osugi, W. Chanmanee, C. R. Chenthamarakshan, M. V. B. Zanoni, P. Kajitvichyanukul and R. Krishnan-Ayer, *J. Photochem. Photobiol., C*, 2008, **9**, 171–192.

16 T. Shahwan, S. Abu Sirriah, M. Nairat, E. Boyacı, A. E. Eroğlu, T. B. Scott and K. R. Hallam, *Chem. Eng. J.*, 2011, **172**, 258–266.

17 Y. Zhao, H. Jiangyong and H. Chen, *J. Photochem. Photobiol., A*, 2010, **212**, 94–100.

18 M. C. Pereira, L. C. A. Oliveira and E. Murad, *Clay Miner.*, 2018, **47**, 285–302.

19 H. Almkhelfe, X. Li, P. Thapa, K. L. Hohn and P. B. Amama, *J. Catal.*, 2018, **361**, 278–289.

20 Z. Song, B. Wang, J. Yu, C. Ma, C. Zhou, T. Chen, Q. Yan, K. Wang and L. Sun, *Appl. Surf. Sci.*, 2017, **413**, 292–301.

21 X. Li, Y. Huang, C. Li, J. Shen and Y. Deng, *Chem. Eng. J.*, 2015, **260**, 28–36.

22 X.-X. Ji, H.-F. Wang and P.-J. Hu, *Rare Met.*, 2018, **38**, 783–792.

23 M. I. Litter and M. Slodowicz, *J. Adv. Oxid. Technol.*, 2017, **20**, 20160164.

24 J. I. Nieto-Juarez and T. Kohn, *Photochem. Photobiol. Sci.*, 2013, **12**, 1596–1605.

25 A. Szecsenyi, G. Li, J. Gascon and E. A. Pidko, *ACS Catal.*, 2018, **8**, 7961–7972.

26 R. B. Wang and A. Hellman, *J. Chem. Phys.*, 2018, **148**, 094705.

27 C. Zhou, H. Yang, D. Qi, J. Sun, J. Chen, Z. Zhang, L. Mao, Z. Song and L. Sun, *Fuel*, 2018, **216**, 513–520.

28 M. B. Robin and P. Day, in *Advances in Inorganic Chemistry and Radiochemistry*, ed. H. J. Emeléus and A. G. Sharpe, Academic Press, 1968, vol. 10, pp. 247–422.

29 J. M. D. Coey, M. Viret and S. von Molnár, *Adv. Phys.*, 1999, **48**, 167–293.

30 H. Wei and E. Wang, *Anal. Chem.*, 2008, **80**, 2250–2254.

31 J. Ahdjoudj, C. Martinsky, C. Minot, M. A. Van Hove and G. A. Somorjai, *Surf. Sci.*, 1999, **443**, 133–153.

32 D. Santos-Carballal, A. Roldan, R. Grau-Crespo and N. H. de Leeuw, *Phys. Chem. Chem. Phys.*, 2014, **16**, 21082–21097.

33 W. C. Bray and M. H. Gorin, *J. Am. Chem. Soc.*, 1932, **54**, 2124–2125.

34 R. Gargallo-Caballero, L. Martin-Garcia, A. Quesada, C. Granados-Miralles, M. Foerster, L. Aballe, R. Bliem, G. S. Parkinson, P. Blaha, J. F. Marco and J. de la Figuera, *J. Chem. Phys.*, 2016, **144**, 094704.

35 X. Li and J. Paier, *J. Phys. Chem. C*, 2016, **120**, 1056–1065.

36 D. Santos-Carballal, A. Roldan, R. Grau-Crespo and N. H. de Leeuw, *Phys. Chem. Chem. Phys.*, 2014, **16**, 21082–21097.

37 T. Yang, X.-d. Wen, J. Ren, Y.-w. Li, J.-g. Wang and C.-f. Huo, *J. Fuel Chem. Technol.*, 2010, **38**, 121–128.

38 C. Zhou, B. Wang, Z. Song, C. Ma, J. Yu, Z. Zhang, H. Yang and L. Sun, *Fuel*, 2017, **202**, 318–327.

39 Y. Xu, H. Hao, P. Liu, Q. Wang, Y. Sun and G. Zhang, *CrystEngComm*, 2014, **16**, 10451–10459.

40 G. Kresse and J. Furthmüller, *Comput. Mater. Sci.*, 1996, **6**, 15–50.

41 G. Kresse and J. Furthmüller, *Phys. Rev. B: Condens. Matter Mater. Phys.*, 1996, **54**, 11169–11186.

42 G. Kresse and J. Hafner, *Phys. Rev. B: Condens. Matter Mater. Phys.*, 1993, **47**, 558–561.

43 G. Kresse and J. Hafner, *Phys. Rev. B: Condens. Matter Mater. Phys.*, 1994, **49**, 14251–14269.

44 J. P. Perdew, K. Burke and M. Ernzerhof, *Phys. Rev. Lett.*, 1996, **77**, 3865–3868.

45 P. E. Blöchl, *Phys. Rev. B: Condens. Matter Mater. Phys.*, 1994, **50**, 17953–17979.

46 G. Kresse and D. Joubert, *Phys. Rev. B: Condens. Matter Mater. Phys.*, 1999, **59**, 1758–1775.

47 T. K. Ng and P. A. Lee, *Phys. Rev. Lett.*, 1988, **61**, 1768–1771.

48 R. Zimmermann, P. Steiner, R. Claessen, F. Reinert, S. Hüfner, P. Blaha and P. Dufek, *J. Phys.: Condens. Matter*, 1999, **11**, 1657–1682.

49 J. Klimeš, D. R. Bowler and A. Michaelides, *Phys. Rev. B: Condens. Matter Mater. Phys.*, 2011, **83**, 195131.

50 H. J. Monkhorst and J. D. Pack, *Phys. Rev. B: Solid State*, 1976, **13**, 5188–5192.

51 G. Henkelman, B. P. Uberuaga and H. Jónsson, *J. Chem. Phys.*, 2000, **113**, 9901–9904.

52 N. T. H. Kim-Ngan, W. Soszka and A. Kozłowski, *J. Magn. Magn. Mater.*, 2004, **279**, 125–133.

53 H. Shagholani, S. M. Ghoreishi and M. Mousazadeh, *Int. J. Biol. Macromol.*, 2015, **78**, 130–136.

54 K. Mathew, R. Sundararaman, K. Letchworth-Weaver, T. A. Arias and R. G. Hennig, *J. Chem. Phys.*, 2014, **140**, 084106.

55 K. Mathew, V. S. C. Kolluru, S. Mula, S. N. Steinmann and R. G. Hennig, *J. Chem. Phys.*, 2019, **151**, 234101.